



# Influence of cellulose nanocrystal/sisal fiber on the mechanical, thermal, and morphological performance of polypropylene hybrid composites

Jyoti Agarwal<sup>1</sup> · Smita Mohanty<sup>1</sup> · Sanjay K. Nayak<sup>1</sup>

Received: 28 October 2019 / Revised: 5 February 2020 / Accepted: 19 March 2020 /

Published online: 26 March 2020

© Springer-Verlag GmbH Germany, part of Springer Nature 2020

## Abstract

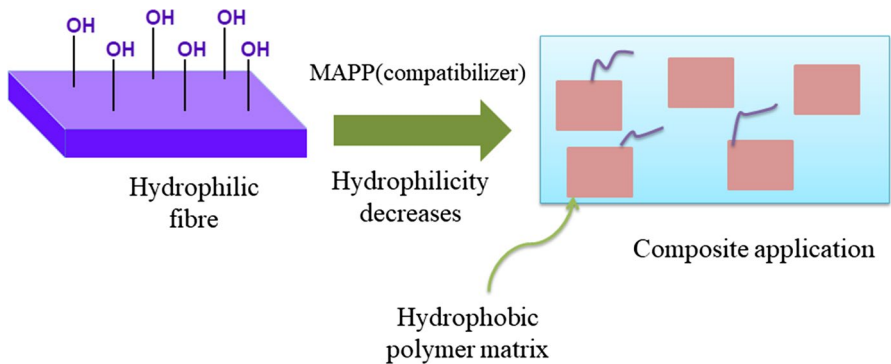
Polypropylene (PP)/sisal fiber (SiF)/cellulose nanocrystals (CNC) hybrid composites were prepared at a variable weight percentage of SiF/CNC loading (29:1, 27:3, 25:5, and 23:7) using melt-blending technique followed by injection molding. The dispersion of the CNCs and SiFs within the nonpolar PP matrix was enhanced by using maleic anhydride grafted PP (MAPP) as a compatibilizer. Furthermore, the mechanical properties like tensile, flexural, and impact properties of the hybrid composites were evaluated. High tensile strength and modulus of 47.02 MPa and 2820.26 MPa, respectively, were observed for the hybrid composite with the incorporation of SiF/CNC (27:3 wt%) in the presence of 5 wt% MAPP. Additionally, an increment of 30.87% and 14.81% was observed for corresponding flexural strength and modulus as compared to their counterparts without MAPP. The elastic moduli obtained experimentally were compared with the theoretical elastic moduli using Cox–Krenchel and Ouali model in combination with the Halpin–Tsai model. Surface morphology by field emission scanning electron microscopy observed that the CNCs and SiFs were well dispersed within the PP matrix in the presence of MAPP. Differential scanning calorimetry thermograms showed no measurable changes in the melting temperature ( $T_m$ ) of PP in PP hybrid composites; however, an increment in the crystallization temperature ( $T_c$ ) was observed. The thermogravimetric analysis confirmed the enhancement in the thermal stability of PP hybrid composites due to the synergistic effect of hybridization within the PP matrix. Partial substitution of CNCs along with SiFs within the matrix polymer shows an increment in the stiffness of the hybrid composites as evident by dynamic mechanical analysis.

---

✉ Jyoti Agarwal  
jyoti886@gmail.com

<sup>1</sup> Laboratory for Advanced Research in Polymeric Materials (LARPM), School for Advanced Research in Polymers (SARP), Central Institute of Plastics Engineering and Technology, CNIC B-25, Patia, Bhubaneswar, Odisha 751024, India

## Graphic abstract



**Keywords** Polypropylene · SiF · CNC · MAPP · FESEM

## Introduction

The demand for lightweight and tougher materials have gained considerable momentum in automobile, aeronautics, building, and construction industries to improve the reliability, durability, and efficiency of the structural components. Composite materials have demonstrated the desired performance characteristics with respect to their improved durability as well as mechanical strength. Natural-fiber-reinforced polymeric composite (NFPC), owing to their low density, high strength, and rigidity, have attracted the key industrial sectors [1–3]. Natural fibers like jute, sisal, kenaf, bamboo, etc., are excellent substitute for synthetic counterparts like glass, talc, mica, etc., in terms of properties like renewability, durability, and low cost which warrant their potentiality for the aforementioned applications across the globe [4].

Among the broadly classified natural fibers, SiF has been the most preferred reinforcing agent in polymer matrices because of its excellent stiffness and tensile strength in the composite application. The chemical composition of SiF constitutes of three major components: cellulose (47–62 wt%), lignin (7–9 wt%), and pentosan (21–24 wt%) (Kaewkuk et al. [5]). A preliminary study as confirmed from Joseph et al. [6] described that SiF-reinforced thermoplastic matrix achieves better properties than the wood fibers in terms of high impact strength. Mohanty et al. [7] investigated the mechanical, thermal, and viscoelastic properties of SiF-reinforced PP composite in the presence of MAPP. The studies revealed that the incorporation of 21 volume% of fibers and 1 wt% of MAPP within the PP matrix displayed optimum mechanical properties along with improved thermal stability. PP has been the widely used thermoplastic matrix for the production of large-volume parts with numerous advantages like good stiffness, easy availability, design flexibility, recyclability, low

cost, and excellent weathering resistance [8, 9]. Literature survey pertaining to the use of various natural-fiber-reinforced PP composites has been reported using sisal, jute, bamboo, kenaf, etc. [10–13].

CNCs isolated from various natural sources/fibers are evolving as smart nanomaterials, comprising of several crystalline allomorphs. CNCs possess properties like high surface area, aspect ratio, and specific strength, along with non-toxicity and inherent biodegradability characteristics [14]. CNC-reinforced PP nanocomposites have been widely used in different prospective end-use applications due to low wear and tear in machinery, recyclability, versatility, and reduced carbon footprints [15, 16]. Ayaz et al. [15] reported the mechanical and thermal analysis of cellulose nanowhisker-reinforced PP nanocomposites. The authors reported that the nanocomposites depicted improved thermal stability and tensile strength to the tune of 70–80% as compared to the PP matrix. Jae et al. [17] studied the mechanical and physicochemical properties of PP/CNC nanocomposites in the presence of MAPP and toluene diisocyanate (TDI). The authors observed that the thermal stability and tensile properties of TDI-grafted CNC/PP nanocomposites are lower than that of MAPP-grafted counterparts.

However, irrespective of these attractive properties, few disadvantages are also associated with natural fibers which include high moisture content in the fiber, poor dispersion, and incompatibility with the polar matrix, consistency in the properties as compared to their synthetic counterparts. In order to increase the mechanical performance, hybridization of fibers is an effective tool in increasing the usage of natural fibers in composite applications. A lot of development on cellulosic/cellulosic natural-fiber-based hybrid composites have been reported which includes sawdust/sisal, wood flour/sisal, banana/sisal, jute/manmade cellulose fibers, etc. [18–21]. Mubarak et al. [19] studied the mechanical and morphological properties of jute/manmade cellulose fiber-reinforced PP hybrid composites. The authors reported that a balanced property profile is achieved by the addition of 25 wt% of jute and 75 wt% of manmade cellulose into the composites with an increase in the stiffness and heat deflection properties [22]. Similarly, several reports in the area of natural fiber/glass PP hybrid composites have been reported widely [10, 12]. Also, studies on cellulosic/cellulosic hybrid composites in thermoset matrices have been reported by various researchers [23, 24]. In the current study, attempts have been made to improve the performance of hydrophobic PP matrix by reinforcing with natural fibers to fabricate lightweight parts for automotive applications such as door panels, interior trims, arm rests, bumpers. The reduction in the vehicle's weight helps to increase the fuel efficiency with reduced CO<sub>2</sub> footprints [25]. Farah et al. [26] reported that the utilization of natural fibers in composites has been tremendously increased over the years to obtain lightweight automotive products with more suitable cost-effective techniques.

The present research makes an effort to prepare PP hybrid composite using SiFs and CNCs as reinforcing agents. To enhance the interfacial adhesion, MAPP has been used as a compatibilizer at variable wt% for the fabrication of the hybrid composites. To the best of our knowledge, this is a distinct methodology for the addition of CNCs in nanosize along with SiFs in microsize and its fabrication for the

formation of hybrid PP/CNC/SiF composites. The synergistic effect of hybridization on the mechanical, thermal, morphological, flammability, and viscoelastic properties of the composites has been reported.

## Experimental

### Materials

PP (Grade: M110) obtained from M/s Haldia Petrochemicals (Kolkata, India) with a density of 0.9 g/cm<sup>3</sup>, a molecular weight of ~250,000 g/mol, and MFI of 11 g/10 min at 2.16 kg load and 230 °C was used as the base matrix. CNCs in powder form (density 1.6 g/cm<sup>3</sup>, purity 99.9, length 0.7 μm, and diameter 10–40 nm) were obtained from M/s Nanoshel (Punjab, India). SiFs (density 1.35 g/cm<sup>3</sup>, length 3–7 mm, and diameter 0.2–0.4 mm) were procured from M/s Gogreen Products (Chennai, India). MAPP with the acid number 15 mg KOH/g, Grade G-3015, and MFI of 32 g/min was procured from M/s Eastman Chemicals Pvt Ltd (Hyderabad, India) was used as a compatibilizer.

### Fabrication of hybrid composite

Initially, the SiF bundles were washed with a mild detergent solution followed by washing with distilled water to remove the wax content and other impurities present in it. Thereafter, they were allowed to dry under sunlight for 48 h and chopped to 3–7 mm length. Prior to the fabrication of composites, the SiFs and CNCs were subjected to pre-drying in a vacuum oven at 70 °C for 2 h.

PP/SiF/CNC hybrid composites were formulated at different weight% of SiF and CNC loading (29:1, 27:3, 25:5, 23:7) employing melt-blending technique using a batch mixer (M/s Haake Rheomex OS PTW16, Germany). The mixing process was carried out at a temperature of 170 °C, speed of 50 rpm for 15 min. Finally, the melt mixes collected from the batch mixer were subjected to injection molding using a mini injection jet (X-plore 15 ml DSM, TA instruments, the Netherlands) to prepare test specimens following their respective ASTM-D standard. The injection-molding process was carried out at an injection temperature, pressure, and mold temperature of 190 °C, 9 bar, and 35 °C, respectively. A similar procedure was followed to fabricate compatibilized hybrid composites PP/SiF/CNC/MAPP at various wt% of MAPP (1, 3, 5, and 7). For comparative studies, the PP/CNC nanocomposites with and without MAPP were also prepared using the same melt-blending technique followed by injection molding at similar process parameters. The optimized formulations of PP/CNC nanocomposites and detailed preparations of hybrid composites along with its sample codes are summarized in Table 1.

**Table 1** Sample type and its respective code for PP/CNC nanocomposites and PP/SiF/CNC hybrid nanocomposites at the varying ratio with and without MAPP

Sample type	Sample code	SiF content (%)	CNC content (%)	MAPP content (%)
PP	PP	–	–	–
PP/CNC <sub>3</sub>	PPC3	–	3	–
PP/CNC <sub>3</sub> /MAPP <sub>5</sub>	PPC3M5	–	3	5
PP/SiF <sub>29</sub> /CNC <sub>1</sub>	PPS29C1	29	1	–
PP/SiF <sub>27</sub> /CNC <sub>3</sub>	PPS27C3	27	3	–
PP/SiF <sub>25</sub> /CNC <sub>5</sub>	PPS25C5	25	5	–
PP/SiF <sub>23</sub> /CNC <sub>7</sub>	PPS23C7	23	7	–
PP/SiF <sub>27</sub> /CNC <sub>3</sub> /MAPP <sub>1</sub>	PPS27C3M1	27	3	1
PP/SiF <sub>27</sub> /CNC <sub>3</sub> /MAPP <sub>3</sub>	PPS27C3M3	27	3	3
PP/SiF <sub>27</sub> /CNC <sub>3</sub> /MAPP <sub>5</sub>	PPS27C3M5	27	3	5
PP/SiF <sub>27</sub> /CNC <sub>3</sub> /MAPP <sub>7</sub>	PPS27C3M7	27	3	7

### Characterization techniques

#### Mechanical tests

The tensile, impact, and flexural properties of PP, its nanocomposites, and hybrid composites were evaluated as per ASTM-D 638, ASTM-D 256, and ASTM-D 790, respectively. The universal testing machine (UTM, M/s Instron, 3382, UK) was used to conduct the tensile and flexural tests according to their respective ASTM-D standards. For tensile tests, the specimen is prepared in dumb-bell shape with dimensions of 127 mm × 12.7 mm × 3.2 mm. Furthermore, the test was performed at a test speed of 5 mm/min with a gauge length of 50 mm. Similarly, the flexural test was performed at a cross-head speed of 1.3 mm/min while maintaining a span length of 50 mm employing specimens of dimension 125 mm × 12.7 mm × 3.2 mm. Impact properties were determined using an M/s Tinius Olsen, Izod Impact Tester (USA) with samples of dimensions 63.5 × 12.7 × 3 mm. Before conducting the test, a V-shape notch with a depth of 2.54 mm using a notch cutter (Model 899, M/s Tinius Olsen, USA) was made in all the samples. The test was conducted at a laboratory temperature of 23 °C ± 2 °C and 50 ± 5% RH.

#### Heat deflection temperature (HDT)

HDT analysis of virgin PP, its nanocomposites, and hybrid composites were performed using HV-2000A, M/s GoTECH, Taiwan, as per ASTM-D 648. The testing was carried out at a load of 66 Psi with samples of dimension 127 × 12.7 × 3.2 mm.

## Mechanical modeling

The combination of analytical models was employed to calculate the theoretical elastic modulus ( $E_c$ ) of multi-phase hybrid composites. The  $E_c$  of nanoparticle-filled polymer matrix (PP/CNC nanocomposites) was calculated by the Cox–Krenchel and Ouali model, whereas the  $E_c$  of short-fiber-reinforced hybrid composites are evaluated using the Halpin–Tsai equation. Therefore, a series of combined analytical models are used to estimate the theoretical  $E_c$  for PP/SiF/CNC and PP/SiF/CNC/MAPP hybrid composites.

**Cox–Krenchel model** Cox–Krenchel model [27] is used to calculate the elastic modulus of the nanofiller-reinforced polymer composites. Cox [28] incorporated a fiber length efficiency ( $\eta_L$ ) and orientation ( $\eta_0$ ) factor into the “Rule of Mixture” to demonstrate the  $E_c$ . The relation used to calculate  $E_c$  by employing the Cox–Krenchel method is defined in Eq. (1):

$$E_c = (\eta_0 \eta_L E_{\text{CNC}} V_{\text{CNC}}) + (E_m V_m), \quad (1)$$

where

$$\eta_L = 1 - \frac{\tanh(\beta L_{\text{CNC}}/2)}{\beta L_{\text{CNC}}/2}, \quad (2)$$

$$\beta = \frac{2}{d_{\text{CNC}}} \left[ \frac{E_m}{(1-\nu) \ln(\pi/4 V_{\text{CNC}})^{0.5} E_{\text{CNC}}} \right], \quad (3)$$

where  $\eta_0$  value is considered to be 0.375 as per the literature [29],  $L_{\text{CNC}}$  and  $d_{\text{CNC}}$  are the length and diameter of CNC which were measured to be 0.7  $\mu\text{m}$  and 25 nm, respectively, as discussed in “Transmission electron microscopy (TEM)” section.  $V_{\text{CNC}}$  and  $V_m$  are the volume fraction of the CNC and PP matrix, and  $\nu$  is Poisson’s ratio of the matrix. The elastic moduli and density of CNCs were represented by  $E_{\text{CNC}}$  and  $\delta_{\text{CNC}}$ ; additionally, their respective values for the current study were considered to be 88 GPa and 1.54 g/cc in accordance with the literature [30].

**Ouali model** Ouali model is based on the percolation theory and is a revised form of the series–parallel model. It calculates the  $E_c$  by taking into consideration the percolating, non-percolating CNC phase, and the matrix phase. Ouali model assumed a considering factor ( $V_{\text{CNC-C}}$ ) known as the critical volume fraction of CNCs for the formation of percolation network and is calculated as by Eq. (4):

$$V_{\text{CNC-C}} = \frac{0.7}{L_{\text{CNC}}/d_{\text{CNC}}}. \quad (4)$$

The  $E_c$  of the CNC-reinforced PP is given by Eq. (5):

$$E_c = \frac{(1 - 2V_{CNC}\epsilon)E_m E_{CNC} + (1 - V_f)\epsilon E_{CNC}^2}{(1 - V_{CNC})E_{CNC} + (\epsilon - V_{CNC})E_m} \tag{5}$$

where  $\epsilon = 0$ , if  $v_{CNC} \leq v_{CNC-C}$

$$\epsilon = v_{CNC} \left( \frac{V_{CNC} - V_{CNC-C}}{1 - V_{CNC-C}} \right), \text{ if } v_{CNC} > v_{CNC-C}$$

where  $\epsilon$  is represented as the percolation network of the CNC phase.

**Halpin–Tsai model** Halpin–Tsai equation is usually used to demonstrate the  $E_c$  of the composites reinforced with short fibers. Therefore, the  $E_c$  of the hybrid composites is calculated by the Halpin–Tsai equation as detailed below:

$$\frac{E_{Hc}}{E_c} = \frac{1 + \xi\eta V_{SiF}}{1 - \eta V_{SiF}}, \tag{6}$$

where  $\eta$  is calculated as:

$$\eta = \frac{\frac{E_{SiF}}{E_c} - 1}{\frac{E_{SiF}}{E_c} + \xi}, \text{ where } \xi = 2 \frac{l_{cSiF}}{d_{SiF}}. \tag{7}$$

$E_{Hc}$  and  $E_c$  are the calculated theoretical elastic modulus of the hybrid composite and PP/CNC nanocomposite,  $E_{SiF}$ , and  $V_{SiF}$  are the elastic modulus and volume fraction of SiF,  $l_{cSiF}$  and  $d_{fc}$  are the critical fiber length and diameter of SiF, respectively. The  $l_{cSiF}$  is calculated by the equation as described in Eq. (8)

$$l_{cSiF} = \frac{\sigma_{SiF} d_{SiF}}{2}, \text{ where } \sigma = \frac{\sigma_m}{\sqrt{3}} \tag{8}$$

where  $\sigma_{SiF}$  and  $\sigma_m$  are described as the tensile strength of SiF and polymer matrix, and  $\sigma$  is represented as the interfacial shear strength between matrix and fiber.

**Fourier transmission infrared analysis (FTIR)**

FTIR of virgin PP, SiF, and CNC, PP/SiF/CNC, and PP/SiF/CNC/MAPP hybrid composites were examined to study the functional groups and interfacial bonds in the samples using Nicolet 6700 (ThermoFisher, USA). The analysis was carried out at a resolution of  $4 \text{ cm}^{-1}$  followed by 64 numbers of successive scans in wave number range of  $4000\text{--}400 \text{ cm}^{-1}$ .

**X-ray diffraction analysis (XRD)**

XRD analysis of virgin PP, SiF, CNC, and its hybrid composites was performed using an X-ray diffractometer (7000L, Shimadzu, Japan). Cu K $\alpha$  radiation source (20 mA, 40 kV,  $\lambda = 1.54 \text{ \AA}$ ) was used to conduct the test at a rate of  $5^\circ/\text{min}$  and a

range of scanning angle between 5° and 40°. The crystallite size and d-spacing value for every test samples were calculated by employing Scherer's formula and Bragg's equation using Eqs. (9) and (10):

$$\text{Average crystallite size} = \frac{0.89 * \lambda}{w * \cos(\theta)}, \quad (9)$$

$$d = n\lambda/2\sin\theta, \quad (10)$$

where  $\lambda$  and  $\theta$  are denoted as the wavelength of the Cu K $\alpha$  X-ray and diffraction angle, respectively, and  $w$  is the full width at half maximum of diffraction (rad).

### Thermal analysis

Differential scanning calorimetry (DSC) analysis was conducted using DSC Q-20, M/s TA Instruments, USA. At a temperature range of 30–200 °C, samples of  $\leq 7$  mg were heated under a nitrogen atmosphere at a heating rate of 10 °C/min. The existence of any previous thermal history is removed by holding the heated sample at the particular temperature for 1 min and thereafter cooling down to 30 °C to measure the crystallization temperature ( $T_c$ ). Further, the melting temperature ( $T_m$ ) was measured by reheating the samples up to 200 °C. The degree of crystallinity  $X_c$  (%) is evaluated by Eq. (11):

$$X_c (\%) = \frac{\Delta H_m}{\Delta H^*} \times 100\%, \quad (11)$$

where  $\Delta H_m$  is represented as the melting heat of fusion measured by DSC analysis,  $\Delta H^*$  is standard melting heat of fusion of PP matrix whose value is estimated to be 240.5 J/g [3].

Thermogravimetric analysis (TGA) was conducted using TGA Q50, M/s TA instrument, USA, with test specimens of 5–8 mg under the nitrogen atmosphere. The analysis was performed at a temperature range of 30–700 °C while maintaining a flow rate of 30 ml/min and a heating rate of 10 °C/min.

### Dynamic mechanical analysis (DMA)

DMA test was performed with DMA-Q800, M/s TA Instruments, USA, with prismatic samples of dimension 35×12×3 mm under nitrogen atmosphere. The test was carried out at a frequency of 1 Hz and a temperature range of –50 to 150 °C while maintaining a heating rate of 10 °C/min. In all the cases, four samples of each composition were tested, and the mean values of storage modulus ( $E'$ ) and loss tangent ( $\tan \delta$ ) were noted.

### Microscopy studies

**Transmission electron microscopy (TEM)** The diameter and length of CNCs were studied using TEM analysis (JEOL 1400, Japan). Prior to the tests, the suspension



of CNCs was done using an ultrasonication bath for 1 h. Thereafter, a drop from the solution was kept on a copper grid coated with a thin layer of the carbon film. The copper grid was allowed to dry, and the test was performed at operating voltage of 80 kV.

**Field scanning electron microscopy (FESEM)** FESEM analysis of SiF, CNC, and the hybrid composites was carried out to study the impact fractured surface morphology using Sigma, Zeiss, UK. Prior to the tests, all the samples are gold-coated using the sputtering unit (sputter coater, BAL-TEC SCD 050, USA) to avoid any accumulation of electric charge.

### Flammability

The horizontal and vertical flammability properties of virgin PP and its hybrid composites were performed by HVUL 2(M/s Atlas, USA) as per UL-94. The samples with dimension  $125 \times 12.7 \times 3$  mm were used to measure the rate of burning.

## Results and discussion

### Mechanical properties of PP, its nanocomposites, and hybrid composites

The mechanical properties of virgin PP, its nanocomposites, and hybrid composites at the various wt% of SiF, CNC, and MAPP loading are represented in Table 2. In the case of PP/CNC nanocomposites, the optimized samples formulated with and without compatibilizer (PPC3 and PPC3M5) were reported. For hybrid composites, the total SiF and CNC content was fixed at 30% as per the findings of Samal et al. [31] and Kalaprasad et al. [32]. As evident from Table 2, the tensile strength and modulus of PP are 32.62 MPa and 1238 MPa, respectively.

The tensile strength and modulus of PPC3 nanocomposites are 33.90 MPa and 1320.60 MPa which depicted an enhancement of about 3.92% and 6.67%, respectively, as compared to PP matrix. However, there was a substantial increase in the flexural strength and modulus of PP in PPC3 nanocomposites to 41.37% and 30.80%, respectively. Additionally, PPC3 nanocomposites exhibited impact strength of 26.08 J/m that depicted an increment of 20.68% over that of PP estimates. Similarly, the tensile strength and modulus of PPC3 in PPC3M5 revealed enhanced values to the tune of 13.98% and 25.64%, respectively. The addition of 5 wt% of MAPP in PPC3 nanocomposites further increased the flexural strength and modulus by 27.73% and 25.24%, respectively. PPC3M5 showed impact strength of 28.9 J/m which is increased to the tune of 10.8% as compared to PPC3 nanocomposites. The addition of MAPP promotes interfacial adhesion between nonpolar PP matrix and hydrophilic CNCs at the interface, thereby increasing the mechanical properties in the nanocomposites. The hybridization of CNCs with SiFs in the PP matrix resulted in further enhancement of the mechanical properties as summarized in Table 2.

The mechanical properties of PP in PP/SiF/CNC hybrid composites increased consistently up to 27:3 wt% of SiF and CNC loading. Thereafter, a subsequent

**Table 2** Mechanical properties of PP and its hybrid composites

Sample code	Tensile strength (MPa)	Tensile modulus (MPa)	Elongation at break (%)	Flexural strength (MPa)	Flexural modulus (MPa)	Impact strength (J/m)	HDT (°C)
PP	32.62 ± 0.1	1238 ± 34	425 ± 5	30.45	1053.63 ± 30	21.61 ± 0.91	116.9
PPC3	33.90 ± 0.39	1320.60 ± 42.37	102.63 ± 1.34	43.05 ± 0.45	1378.18 ± 99.26	26.08 ± 0.50	117.2
PPC3M5	38.64 ± 0.80	1659.23 ± 36.60	61.65 ± 3.12	54.99 ± 0.71	1726.14 ± 33	28.9 ± 1.02	121.5
PPS29C1	34.06 ± 1.45	2124.22 ± 117.4	5.16	47.45 ± 0.35	2527.35 ± 25	34.36 ± 2.43	132.5
PPS27C3	34.47 ± 0.83	2406.22 ± 147.79	5.05 ± 0.13	54.02 ± 0.04	2884.75 ± 5.50	35.42 ± 2.93	136.8
PPS25C5	33.43 ± 0.63	2236.10 ± 43.47	4.95 ± 0.08	53.03 ± 0.3	2445.51 ± 142.50	32.29 ± 1.27	134.5
PPS23C7	33.69 ± 0.95	2199.14 ± 169.1	4.87 ± 0.12	47.61 ± 1.7	2595.81 ± 280	31.86 ± 3.21	134.1
PPS27C3M1	46.58 ± 1.46	2442.88 ± 35	3.86 ± 0.35	66.36 ± 3.47	2885.15 ± 165	37.55 ± 3.51	142.3
PPS27C3M3	46.81 ± 1.23	2526.09 ± 163	3.78 ± 0.19	69.46 ± 0.33	3083.17 ± 78	38.32 ± 1.04	144.9
PPS27C3M5	47.04 ± 0.30	2820.26 ± 21	3.57 ± 0.50	70.70 ± 0.06	3312.22 ± 41	38.62 ± 2.80	146.3
PPS27C3M7	46.05 ± 0.36	2632.61 ± 424	3.41	69.25 ± 0.11	3008.20 ± 369	37.1 ± 3.36	145.7

reduction was observed with the incorporation of 25:5 and 23:7 wt% of SiF and CNC loading within the PP matrix. PPS27C3 hybrid composite exhibited an optimum tensile strength and modulus of 34.47 MPa and 2406.22 MPa, respectively, which was 5.67% and 94.36% higher than that of the PP matrix. This behavior is possibly due to the synergism in the reinforcing effect of both CNC and SiF within the PP matrix thereby improving the tensile properties. Similar enhancement in the flexural strength and modulus to the tune of 77.40% and 173.79% in the case of PPS27C3 hybrid composite as compared with the matrix polymer was observed. Table 2 reports the impact properties of the hybrid composites, wherein an optimum impact strength of 35.42 J/m was noticed in the case of PPS27C3 hybrid composites, which is around 63.90% higher than that of the PP matrix. However, a drop in the impact strength at 25:5 and 23:7 wt% of SiF and CNC loading was observed for PP/SiF/CNC hybrid composites. At higher loading of CNCs, an increase in the fiber–fiber contact arises within the hybrid composite due to the high surface area of CNCs. This relatively creates multiple paths for the easy propagation of the cracks which attributes in the decrement of mechanical properties at higher CNCs loading [33].

The variation in the mechanical properties as a function of MAPP content (1, 3, 5, and 7 wt%) with optimized PPS27C3 hybrid composite is also given in Table 2. It reported that the incorporation of MAPP up to 5 wt% in PPS27C3 hybrid composite depicted an increment in the tensile strength and modulus to the tune of 36.46% and 17.20%, respectively. Moreover, flexural strength and modulus of PPS27C3M5 hybrid composite exhibited an optimum increment of 30.87% and 14.81% as compared to their counterparts without MAPP. The overall enhancement in tensile and flexural properties for the PP hybrid composites in the presence of MAPP is attributed to the better compatibility effect among the fibers–fillers–matrix. Generally, the anhydride part of MAPP creates bonds with the hydroxyl (OH) groups of CNC and SiF thus forming an ester linkage that creates an effective stress transfer network at the interface [22, 34]. This helps in restricting the polymer matrix chain mobility, which in turn improves the interfacial adhesion between the individual fibers/fillers and PP matrix. Apart from this, chemical interaction like van der Waal's forces and hydrogen bonding also takes place, but their influence for the stress transfer phenomenon is less noteworthy [34]. Therefore, the addition of MAPP acts as a compatibilizer that enhances the dispersibility of CNCs and SiFs within the nonpolar PP matrix. Subsequently, a reduction in tensile and flexural properties was observed at 7 wt% of MAPP in PPS27C3 hybrid composites. With the incorporation of MAPP at higher wt%, they form self-entanglement among themselves without creating covalent linkages with the fillers and fibers. This results in the reduction of mechanical performance by creating slippage at the interface [10]. Moreover, MAPP is a low molecular weight polymer that acts as a plasticizer at higher wt% of loading which in turn decreases the mechanical properties. Furthermore, the addition of MAPP also increases the impact strength by enhancing the compatibility between hydrophilic fibers/fillers and hydrophobic matrix. Impact strength of 38.62 J/m was obtained at 5 wt% of MAPP loading in PPS27C3 hybrid composites showing an increment to the tune of 9.03%. Keener et al. [35] reported similar behavior and described the addition of MAPP results in effective load transfer by increasing the

interfacial fiber/matrix adhesion. Also, the presence of compatibilizer minimizes the formation of microcracks between the fibers/fillers and PP matrix, thereby reducing the probability of crack propagation under an external impact load. However, PPS27C3M7 hybrid composites exhibited a drop in impact strength to the tune of 3.93% as compared to PPS27CM5 hybrid composites [36]. Based on the above observations, PPS27C3 and PPS27C3M5 hybrid composites were optimized for further studies.

The stress–strain behavior of virgin PP; PPC3 and PPC3M5 nanocomposites; and PPS27C3 and PPS27C3M5 hybrid composites are depicted in Fig. 1. In the case of all samples, an elastic deformation was observed initially as shown by the linear portion of the stress–strain behavior. PP matrix exhibits its proportionality limit at 19.87 MPa, and thereafter, it deviates violating Hooke's law. Furthermore, the PP matrix elongates continuously until it breaks, and this phenomenon is indicated as the plastic deformation of the matrix. It represented the ductile behavior of the PP matrix which is reduced by the incorporation of SiFs and CNCs in their filled counterparts, thus revealing brittle characteristics in the case of composites. The change of failure mode (ductile to brittle) is attributed to the increased stiffness of PP in PP composites due to the addition of SiFs and CNCs. Subsequently, the characteristic curves of PPC3 and PPC3M5 nanocomposites revealed a decreased ductile behavior when compared to PP matrix; conversely, they possessed less brittle characteristics (more elongation) than that of hybrid composites. Furthermore, the characteristic curves of PPS27C3 and PPS27C3M5 are similar; however, PPS27C3M5 exhibits higher ultimate tensile strength and low elongation than that of PPS27C3 hybrid composites. The presence of MAPP enhances the interfacial adhesion in PPS27C3M5 hybrid composites thereby reducing the stress concentrations at the interface [3].

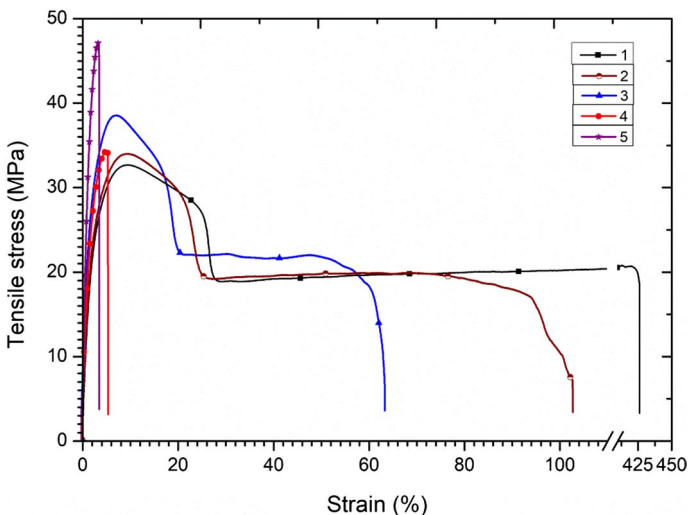


**Fig. 1** Stress–strain curve of (1) virgin PP; (2) PPC3 (3) PPC3M5 nanocomposites; (4) PP S27C3 (5) PPS27C3M5 hybrid composites

HDT of virgin PP; PPC3 and PPC3M5 nanocomposites; and PPS27C3 and PPS27C3M5 hybrid composites is enumerated in Table 2. The PP matrix shows an HDT value of 116.9 °C, which augmented to 117.2 °C and 121.5 °C in the case of PPC3 and PPC3M5 nanocomposites, respectively. Furthermore, PPS27C3 hybrid composites exhibited an HDT value of 136.8 °C that resulted due to increased stiffness by the addition of SiFs and CNCs. Moreover, an optimum HDT value of 146.3 °C was observed in the case of PPS27C3M5 hybrid composite thereby confirming the synergistic hybridization effect of SiFs and CNCs in the presence of MAPP within the PP matrix. The synergistic hybridization effect occurs due to improved stress transfer from the SiFs, combined with CNCs to the PP matrix [37].

**Mechanical modeling**

Figure 2 shows the theoretical and experimental elastic moduli of nanocomposites and hybrid composites calculated using various micromechanical models. For simplicity, it was assumed that there is no interaction between individual CNCs and short SiF fibers within the hybrid composite. Therefore, the  $E_c$  of CNC-filled PP as calculated by Cox–Krenchel (Eq. 2) and Ouali model (Eq. 5) is taken into account

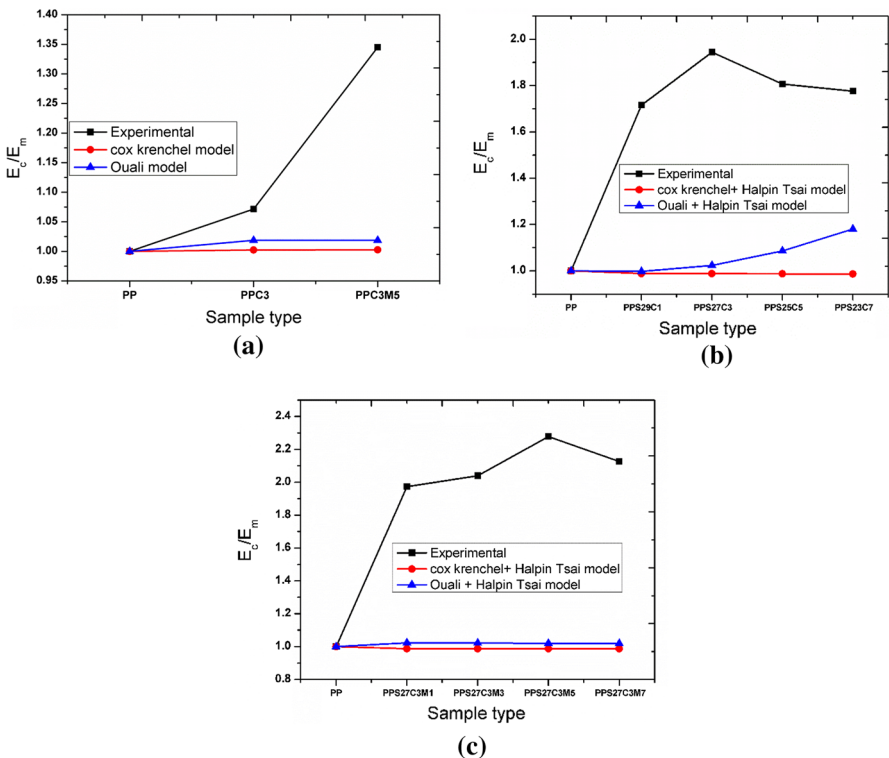


**Fig. 2** Experimental vs. theoretical values using mechanical models **a** PP/CNC nanocomposites; **b** PP/SiF/CNC **c** PP/SiF/CNC/MAPP hybrid composites

as the base matrix for SiF-reinforced PP using the Halpin–Tsai equation (Eq. 6). Fu et al. [38] made a similar assumption for a hybrid composite fabricated by particle-filled short-fiber-reinforced polymer composite. In the case of PPC3, as represented in Fig. 2a, theoretical  $E_c$  as calculated by Ouali and Cox–Krenchel model showed good agreement with experimentally determined values. Thus, the improved  $E_c$  confirms that the CNCs act as a reinforcing agent within the vicinity of the PP matrix as a result of which its stiffness was increased in PPC3 nanocomposites. However, theoretical elastic moduli of PPC3M5 nanocomposites show deviation from the experimentally determined values. This nonconformity in the estimated values of PPC3M5 nanocomposites may perhaps be owed to the inability of both the models to consider the molecular level interactions between the matrix and fillers in the presence of MAPP. Also, the ester linkages developed between the OH group of CNCs and anhydride parts of MAPP were not considered by these mechanical models [27]. In the case of both the hybrid composites as confirmed from Fig. 2b, c, the theoretical modulus using the Cox–Krenchel and Ouali method in combination with the Halpin–Tsai model are not in good agreement with experimental findings and shows a large deviation. Moreover, it was observed that all the combined analytical models underestimate the calculated  $E_c$  as compared with that of experimental values. The nonconformity in the projected values of calculated  $E_c$  by employing various combined analytical models can be explained by similar facts that the models are incompetent to incorporate certain molecular-level interactions as a consequence of aggregation and reinforcing effect between the reinforcing agents and PP matrix. Similar behavior was reported by Prodyut et al. [27] where the authors reported that the incompetence of the analytical models to incorporate the intra- and intermolecular hydrogen bonding among the reinforcing agents leads to a deviation in the theoretically calculated values as compared to its experimentally measured values.

### Fourier transform infrared spectroscopy (FTIR)

FTIR spectra of SiF and CNC are shown in Fig. 3a. It is evident that SiF and CNC reveal an O–H stretching peak at  $3307\text{ cm}^{-1}$  and  $3421\text{ cm}^{-1}$ , respectively; additionally, a peak at  $2897\text{ cm}^{-1}$  was observed that is primarily associated with the C–H stretching. Further, the FTIR spectra of SiF show a peak at  $1736\text{ cm}^{-1}$  that represents the ester linkage due to the presence of P-coumeric and ferulic acids in lignin and hemicellulose. However, the aforementioned peak disappears in the case of CNC due to the absence of lignin and hemicellulose. The vibrational peak at  $1225\text{ cm}^{-1}$  in the case of SiF is associated with the C–O stretching which is absent in the FTIR spectra of CNCs. Moreover, the band at  $1041\text{ cm}^{-1}$  is related to the xylans of hemicelluloses, thereby representing the strong bond of xyloglucans with SiFs and CNCs. FTIR spectra of virgin PP and PPS27C3 and PPS27C3M5 hybrid composites are shown in Fig. 3b. The characteristic peak at  $2952\text{ cm}^{-1}$ ,  $2920\text{ cm}^{-1}$ , and  $2834\text{ cm}^{-1}$  are attributed to the C–H stretching of the PP matrix. Furthermore, the FTIR spectra of the PP matrix depict two more peaks at  $1459\text{ cm}^{-1}$  and  $1369\text{ cm}^{-1}$ , which are associated with the  $\text{CH}_2$  and symmetric  $\text{CH}_3$  deformation, respectively. As evident from FTIR spectra, the hybrid composites with and without MAPP exhibit all the

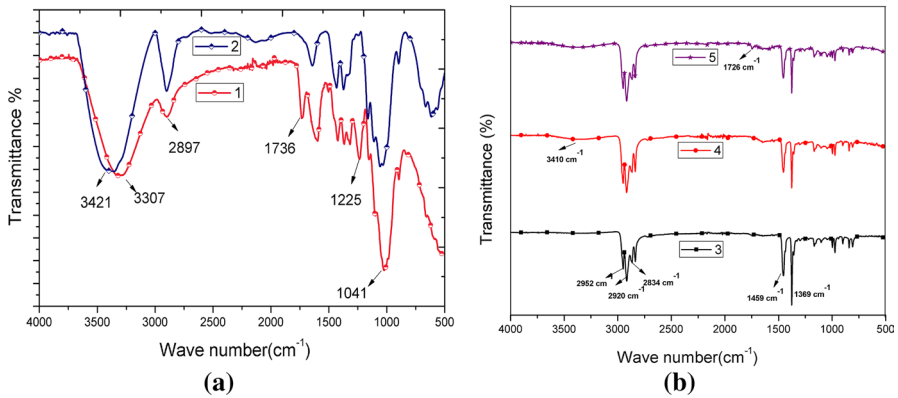


**Fig. 3** FTIR spectra of (1) SiF (2) CNC (3) PP; (4) PPS27C3 (5) PPS27C3M5 hybrid composite

characteristic peaks of PP. Moreover, it depicts a peak at  $3410\text{ cm}^{-1}$  which is related to the O–H stretching of SiFs and CNCs. In the case of PPS27C3M5 hybrid composites, a band at  $1726\text{ cm}^{-1}$  was observed which confirms the formation of ester linkage at the interface. However, this transmittance peak is not visible in the case of PPS27C3 hybrid composites due to the absence of MAPP thereby showing no evidence of the formation of the ester linkage. Biswal et al. [39] corroborated similar findings wherein the authors observed a peak at  $1751\text{ cm}^{-1}$  confirming the formation of ester linkage in PP/pineapple fiber composites at the interface in the presence of MAPP [40].

## Morphology studies

### Transmission electron microscopy (TEM)

CNC shows rod-like fibrillar structure as evident from Fig. 4. As evident from the TEM image by employing ImageJ software, diameter and an average length of the fibrils were found to be about 10–40 nm and 0.7 micrometers, respectively. Furthermore, the aspect ratio ( $L/d$ ) was calculated to be 28. Azeredo et al. [41] reported that  $L/d$  ratio higher than 10 is considered to be a minimum value for any considerable reinforcement to take place within a composite. This additionally confirms an effective stress transfer from the matrix to the fillers at the interface in the composites.

### Field emission scanning electron microscopy (FESEM)

FESEM micrographs of SiF consist of various distinct cells that are composed up together by node-like structures and contain waxy substances on their surface representing a smooth structure (Fig. 5a). On the other hand, CNC signifies rod-like fibrils structure with a smooth and uniform surface as shown in Fig. 5b. The FESEM analysis of impact fractured samples is shown in Fig. 5c, d to evaluate the fracture behavior and fiber–filler–matrix interaction in the case of PPS27C3 and

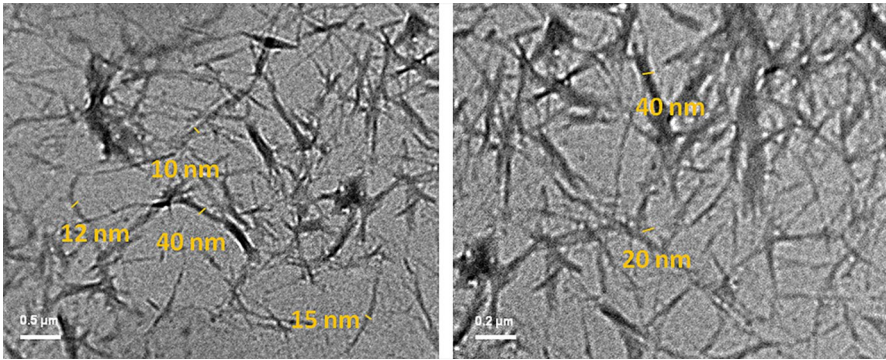


**Fig. 4** TEM images of CNC

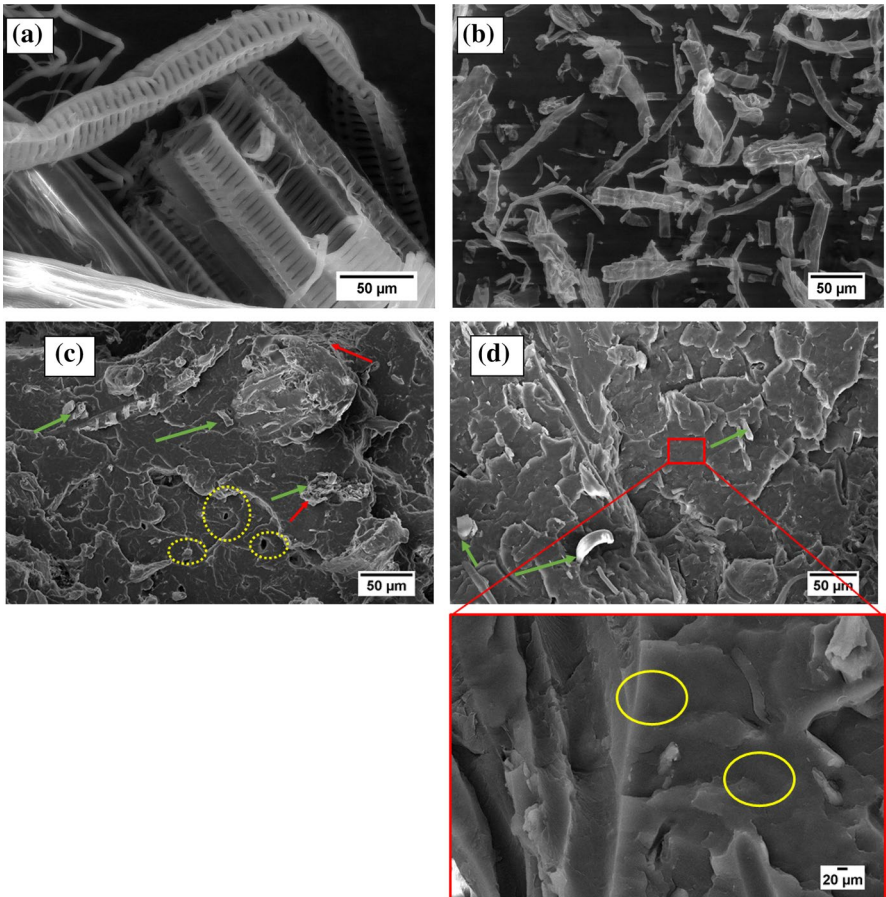


**Fig. 5** Field emission scanning electron micrographs of **a** SiF **b** CNC; **c** PPS27C3 **d** PPS27C3M5 hybrid composites



PPS27C3M5 hybrid composites. The presence of agglomerations (red arrow marks) in the case of PPS27C3 hybrid composites is observed due to the weak interfacial adhesion of SiFs and CNCs within the PP matrix (Fig. 5c). Noticeable small voids and gaps were also seen which indicates the fiber pullouts during the impact fracture (few of them marked by the dotted yellow circle and green arrows). This further confirms the fact that in the case of PPS27C3 hybrid composites, the fiber–filler–matrix interfacial adhesion is not strong enough to avoid the fiber pullouts. However, in the case of PPS27C3M5 hybrid composites, there were absence of holes and gaps as observed from Fig. 5d. This reveals strong fiber–filler–matrix interfacial adhesion achieved in the presence of MAPP which in turn increased the mechanical properties when compared to its counterparts without MAPP. Basheer et al. [24] reported similar studies while investigating the morphological analysis of palm filler-reinforced epoxy composites. The author's observed that the poor matrix/filler interfacial bonding leads to voids/microcracks that affect the mechanical strength of the composites. Moreover, the fibers along with fillers seemed practically embedded within the PP matrix in Fig. 5d (marked by yellow circle marks). This behavior is indicative of the uniform distribution of both SiFs and CNCs within the PP matrix [42]. Although Table 1 represents an increase in the mechanical properties of PPS27C3M5 composites when compared to their counterparts fabricated without the addition of MAPP, some of the fiber pullouts were still observed (marked by the green arrows). The improvement in the mechanical properties can be ascribed to the enhanced interfacial adhesion of the hybrid composites at the interface in the presence of MAPP; however, it seems the fiber–filler–matrix interaction is still less to evade the fiber pullouts. Furthermore, another reason for the fiber pullouts may be ascribed to the mean fiber length which may be less than that of the critical fiber length of the composites. This factor can cause the fiber pullout during the impact fracture instead of a breakage phenomenon, and the similar findings were reported by Rupam et al. [22].

### X-ray diffraction analysis (XRD)

XRD of virgin PP, SiF, and CNC and PPS27C3 and PPS27C3M5 hybrid composites is given in Fig. 6a, b. The diffraction pattern of SiF and CNC as shown in Fig. 6a revealed a broad peak at  $2\theta = 15.3^\circ$  and a sharp peak at  $2\theta = 22^\circ$ , which is ascribed to the amorphous and crystalline characteristics, respectively. The corresponding crystallographic planes associated with the aforementioned peaks are (110) and (002). Besides, CNC depicts one more peak at  $2\theta = 34^\circ$  related to the crystallographic plane corresponding to (004). Figure 6b depicts four major peaks portraying the  $\alpha$ -crystal form of PP at the scattering angle  $13.9^\circ$ ,  $16.67^\circ$ ,  $18.45^\circ$ , and  $21.44^\circ$  having an interlayer d-spacing of 6.28 Å, 5.30 Å, 4.81 Å, and 4.20 Å, respectively, as calculated by Bragg's relation (Eq. 10). The successive diffraction plane associated with the aforementioned diffraction peaks are (110), (040), (130), and (111) [21]. PPS27C3 and PPS27C3M5 hybrid composites exhibit the characteristic peaks of PP except at  $18.45^\circ$  which is not distinctly visible. Additionally, it also depicted the diffraction peak associated with SiF and CNC at  $15.2^\circ$  and  $22^\circ$ . The  $X_c$  (%) for PP, SiF, and CNC was found to be 64.13%, 68.2%, and 75.3%, respectively. Moreover,

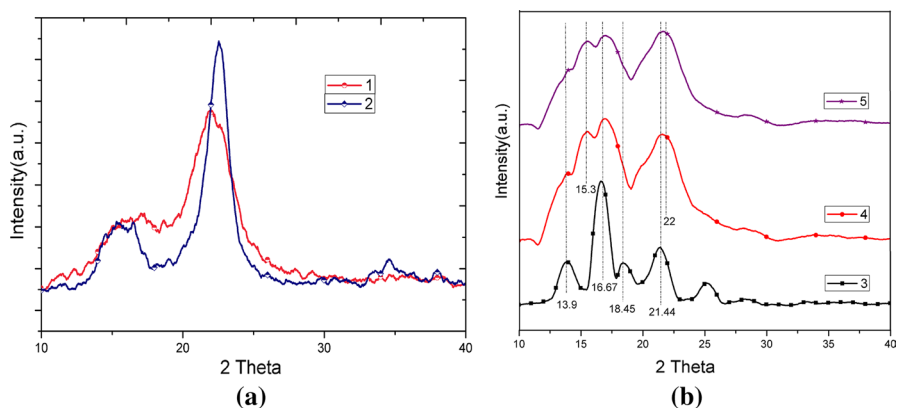


**Fig. 6** X-ray diffraction spectra of (1) SiF (2) CNC (3) PP; (4) PPS27C3 (5) PPS27C3M5 hybrid composite

PPS27C3 and PPS27C3M5 hybrid composites exhibit  $X_c$  (%) of about 61.8% and 60.5%, respectively. This decrement in the  $X_c$  (%) can be explained by the fact that the addition of CNCs and SiF within the PP matrix acts as a nucleating agent, leading to the formation of several numbers of small crystal nuclei within an insufficient space. This restricts the polymer chain mobility which in turn creates crystalline defects and stress among them [43].

The SiFs and CNCs effect on the average crystallite sizes of PP hybrid composites is higher as compared to the PP matrix. The crystalline network of PP in PP hybrid composites is affected by the increased crystalline size which is also corroborated by the DSC analysis explained in “[Differential scanning calorimetry \(DSC\)](#)” section. As reported in Table 3, PPS27C3 showed the optimum crystallite size as compared to PP matrix and PPS27C3M5 hybrid composite that may be due to the weak interfacial adhesion resulting in the inadequate stress transfer from the SiFs; combined with CNCs to the PP matrix [44].

### Differential scanning calorimetry (DSC)

DSC heating and cooling thermograms of virgin PP and PPS27C3 and PPS27C3M5 hybrid composites are shown in Figs. 7 and 8 and summarized in Table 4. As

**Table 3**  $X_c$  (%) and average crystallite sizes (nm) for PP, SiF, CNC, and its hybrid composites

Sample code	Average crystallite sizes (nm)	$X_c$ (%)
SiF	42.03	68.2
CNC	20.68	75.3
PP	30.60	64.13
PPS27C3	45.36	61.8
PPS27C3M5	40.22	60.5

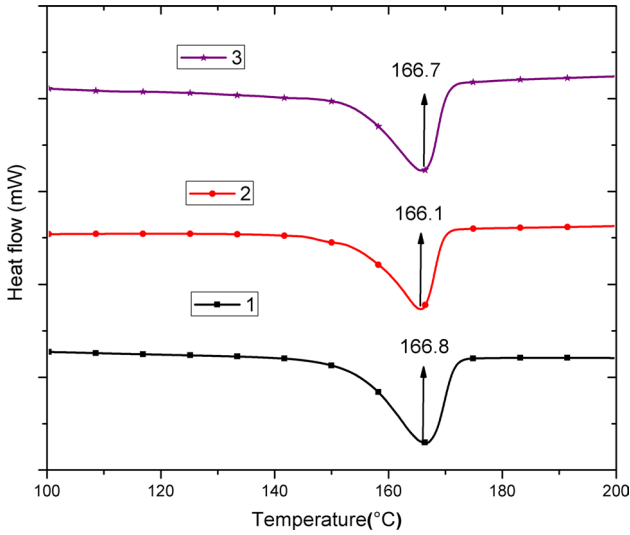


Fig. 7 DSC heating thermogram of (1) PP; (2) PPS27C3 (3) PPS27C3M5 hybrid composite

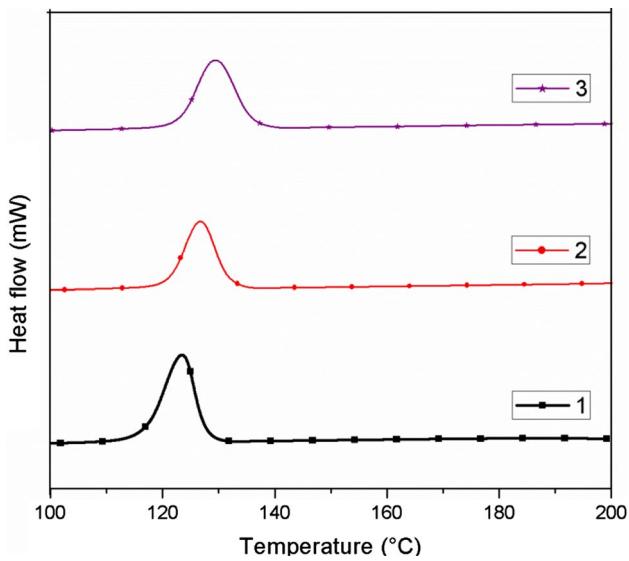


Fig. 8 DSC cooling thermogram of (1) PP; (2) PPS27C3 (3) PPS27C3M5 hybrid composite

**Table 4** DSC analysis of PP and its hybrid composites

Sample code	$T_m$ (°C)	$T_c$ (°C)	$\Delta H_m$ (°C)	$X_c\%$
PP	166.8	122	94.08	39.12
PPS27C3	166.1	126	61.40	25.53
PPS27C3M5	166.7	129	56.42	23.45

depicted in Fig. 7, no appreciable changes were observed in the melting temperature ( $T_m$ ) of PP and its hybrid composites. Nayak et al. [12] reported similar observations in the case of bamboo/glass fiber-reinforced PP hybrid composites. However, an increment in the crystallization temperature ( $T_c$ ) was observed from the DSC cooling thermograms (Fig. 8) with the incorporation of SiFs and CNC within the PP matrix. The  $T_c$  of PP matrix was found to be 123 °C which increased to 126 °C and 129 °C in the case of PPS27C3 and PPS27C3M5 hybrid composites. This enhancement in the  $T_c$  is possibly due to the addition of SiFs and CNCs that restricts the mobility of PP chains at the interface [21]. Moreover, the linear crystalline portion of the PP matrix was interrupted by the incorporation of SiF and CNC leading to a reduction in the  $X_c$  (%). The  $X_c$  (%) for all the samples is determined by using Eq. (11) and is tabulated in Table 4. The  $X_c$  (%) for PPS27C3 hybrid composites was found to be 25.53% which was lower than that of the PP matrix (39.12%). The inclusion of MAPP in PPS27C3M5 hybrid composite results in a decrease in  $X_c$  (%) to about 23.45%. The SiFs and CNCs within the PP matrix act as a nucleating agent thereby resulting in the formation of several nuclei in a limited space. This, in turn, contributed to crystalline defects and stress among the crystals while restricting the molecular motion of the polymer chain [31].

### Thermogravimetric analysis (TGA)

The thermal stability of PP, SiF, CNC and its hybrid composites were investigated from the TGA thermograms depicted in Fig. 9a, b. Table 5 reports the initial degradation temperature ( $T_i$ ), degradation temperature at 10% ( $T_{10}$ ) and 50% ( $T_{50}$ ) weight loss, and final degradation temperature ( $T_f$ ). As seen from TGA thermograms (Fig. 9b), PP matrix displays a single-step degradation behavior showing  $T_i$ ,  $T_{10}$ ,  $T_{50}$ , and  $T_f$  at 340 °C, 353 °C, 381 °C, and 445 °C, respectively. It can be explained by the facts that in the case of the PP matrix, the random scission occurs at higher temperature due to the presence of C–C bonds allowing the thermal degradation

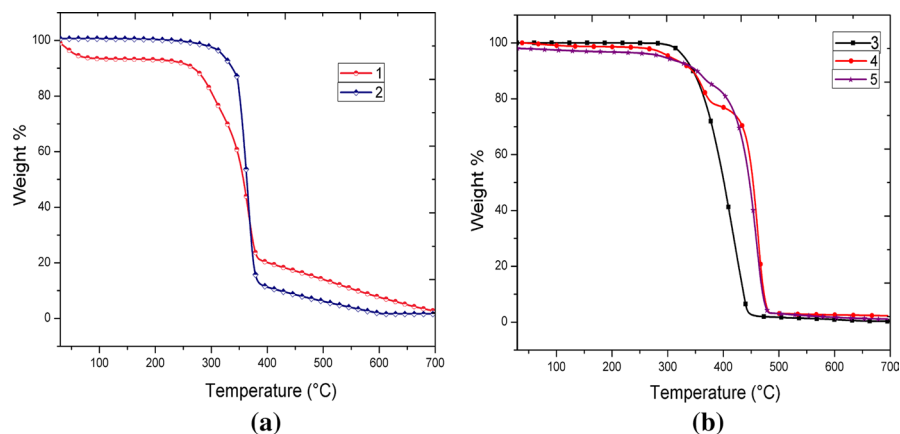


**Fig. 9** TGA thermogram of (1) SiF (2) CNC (3) PP; (4) PPS27C3 (5) PPS27C3M5 hybrid composite

**Table 5** Thermogravimetric analysis of PP, SiF, CNC, and its hybrid composites

Sample code	$T_i$ (°C)	$T_{10\%}$ (°C)	$T_{50\%}$ (°C)	$T_f$ (°C)	Residues after 550 °C (%)
SiF	240	267	357	383	18
CNC	310	340	369	385	7
PP	320	353	381	445	2
PPS27C3	268	344	453	480	4
PPS237C3M5	279	372	454	482	6

to occur at the weak sites [45]. As evident from Table 5, CNCs and SiFs have an onset degradation temperature ( $T_i$ ) and final degradation temperature ( $T_f$ ) of 273 °C, 240 °C and 382 °C, 361 °C, respectively, with a maximum degradation temperature at ~350 °C (Fig. 10a).

The residual mass retention/char residue in the case of CNCs and SiFs approximated to be ~18% and ~7% at 550 °C. Jue et al. [46] studied the degradation of cellulose is primarily because of inter- and intramolecular dehydration reaction. In the case of PPS27C3 hybrid composite, the corresponding  $T_i$ ,  $T_{10}$ ,  $T_{50}$ , and  $T_f$  occurs at 268 °C, 344 °C, 453 °C, and 480 °C. As seen in Fig. 10b, it shows two-step degradation behavior with an initial weight loss at ~330 °C corresponding to the degradation of the SiFs and CNCs. Conversely, the second weight loss at ~460 °C signifies the thermal degradation of virgin PP. The thermal stability of PP in PPS27C3M5 hybrid composites increases due to the synergistic effect of the SiF fibers and CNC fillers within the PP matrix in the presence of MAPP. The  $T_i$ ,  $T_{10}$ ,  $T_{50}$ , and  $T_f$  of PPS27C3M5 hybrid composites occurs at 279 °C, 372 °C, 454 °C, and 482 °C, respectively. On the contrary, the careful examination of the TGA data reveals the untreated PPS27C3 has slightly lower stability than that of PPS27C3M5 hybrid composites. It can be explained by the similar facts that the use of MAPP reduces the number of hydroxyl groups by the formation of esterification linkage thereby revealing greater thermal stability [47]. PPS27C3M5 hybrid composites also show a

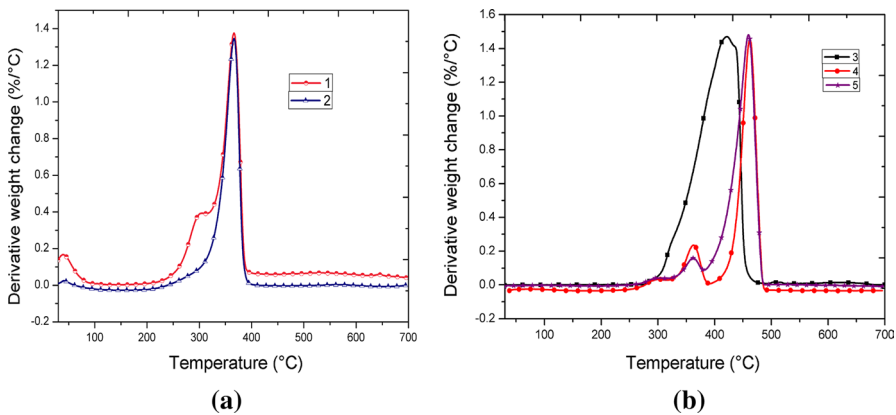


**Fig. 10** DTG thermogram of (1) SiF (2) CNC (3) PP; (4) PPS27C3 (5) PPS27C3M5 hybrid composite

two-step degradation behavior as similar to its counterparts without MAPP. Therefore, SiF and CNC enhance the thermal stability by performing as a heat barrier over the PP matrix consequently giving rise to the formation of char residue after the thermal decompositions. Samal et al. [10] reported similar findings, and the authors described that the presence of fibers/fillers within the PP matrix displayed higher char residue, which indicates improved flame retardancy of PP in PP hybrid composites.

## Dynamic mechanical analysis (DMA)

### Storage modulus ( $E'$ )

Figure 11 shows the variation of  $E'$  as a function of the temperature of PP and its hybrid composites. The  $E'$  exhibits a decreasing trend with an increase in temperature for all the samples. Additionally,  $E'$  depicts a significant fall for all the samples between  $-13\text{ }^{\circ}\text{C}$  and  $10\text{ }^{\circ}\text{C}$  that is associated with the glass transition temperature ( $T_g$ ) region of the PP matrix. Moreover, it was observed that  $E'$  drops steeply in the case of the PP matrix with an increase in temperature owing to the enhanced segmental mobility of polymer chains [48]. However, the addition of SiF and CNCs within the PP matrix with and without MAPP decreases the rate of fall of  $E'$  with the increase in temperature, which indicates the higher stability of PP in PP hybrid composite systems. The  $E'$  value of PP matrix at  $-25\text{ }^{\circ}\text{C}$  was found to be 3900 MPa, which increased to 4700 MPa for PPS27C3 hybrid composites. This behavior can be explained because of the reinforcing effect imparted by SiF and CNCs [49]. Further, PPS27C3M5 hybrid composites exhibited an  $E'$  value of 5200 MPa at  $-25\text{ }^{\circ}\text{C}$  that

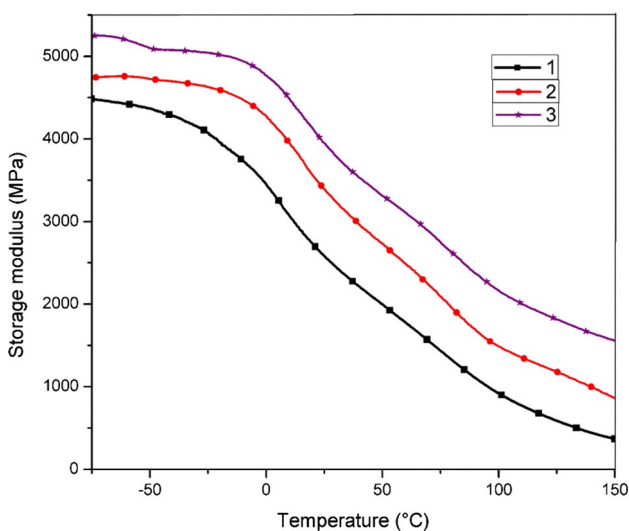
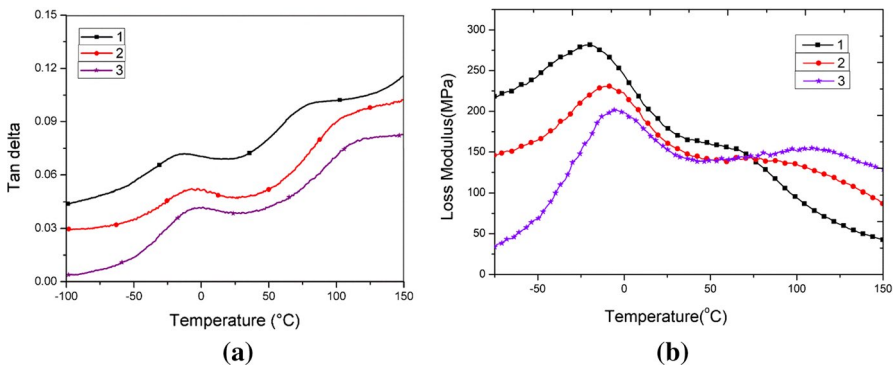


Fig. 11 Variation of  $E'$  versus temperature of (1) PP; (2) PPS27C3 (3) PPS27C3M5 hybrid composite

possibly due to the synergistic hybrid effect of SiF and CNCs within the PP matrix in presence of MAPP.

### Loss tangent ( $\tan \delta$ ) and loss modulus ( $E''$ )

Figure 12a, b shows the effects of hybridization on the  $\tan \delta$  and  $E''$ , respectively.  $\tan \delta$  or loss factor curve is the ratio of  $E''$  (viscous response) to  $E'$  (elastic response). PP matrix exhibits its  $\beta$  and  $\alpha$  relaxation peak around  $-12^\circ\text{C}$  and  $75^\circ\text{C}$ , respectively. The  $\beta$ -transition is related to the  $T_g$ , whereas the  $\alpha$ -transition is attributed to the rotation and lamellar motions of the crystalline phase. The  $\tan \delta$  intensities of both  $\beta$ - and  $\alpha$ -relaxation peak reduced significantly in the case of PPS27C3 and PPS27C3M5 hybrid composites. A slightly positive shift in  $T_g$  of PP in hybrid composites was observed. This effect can be described by the synergistic interaction between SiFs and CNCs within the PP matrix which resulted in the positive shift of  $T_g$  [50]. The decreased intensities are related to the dissipation of vibrational energy due to the less weight fraction of the PP matrix. In the case of hybrid composites, increasing the fibers filler content reduces the  $\tan \delta$  value as it enforces restrictions in the molecular chain mobility of the PP matrix. It resulted due to the adsorption of PP matrix on the surface of the fibers/fillers thereby decreasing viscous response ( $E''$ ) as indicated in Fig. 12b and enhancing the elastic response ( $E'$ ) of the hybrid composite. Gupta et al. [23] studied similar behavior by interpreting the  $E''$  curve where  $T_g$  is shifted toward the positive side of the composites when compared to their parent material, whereas the highest shift was found in the case of hybrid composites. Moreover, PPS27C3M5 hybrid composites revealed the lowest  $\tan \delta$  value as compared to PP matrix and PPS27C3 hybrid composites that are indicative of enhanced fiber–filler–matrix adhesion at the interface. Kitano et al. [51] corroborated similar findings and explained that lower damping factor at the fiber/matrix interface will result in higher interfacial adhesion and vice versa. As evident from Fig. 12a,  $\alpha$ -relaxation peak broadens in case of PPS27C3 and PPS27C3M5 hybrid composites, which



**Fig. 12 a, b** Variation of  $\tan \delta$  and  $E''$  versus temperature of (1) PP; (2) PPS27C3 (3) PPS27C3M5 hybrid composite

**Table 6** Flammability properties (UL-94) of PP and its hybrid composites

Sample	Rate of burning (mm/min.)	Burning behavior
PP	29.12	Continuously burns while producing smoke with an orange-yellow flame, ignites the cotton, and fast dripping was observed
PPS27C3	27.87	It produces smoke while burning with an orange-yellow flame, ignites cotton, and dripping behavior was observed
PPS27C3M5	25.65	Dripping, ignite the cotton, continuously burns with slight smoke and produces an orange-yellow flame

may possibly due to retardation of lamellar motion associated with the crystalline phase of PP matrix by the incorporation of SiFs and CNCs [52].

### Flammability (UL-94)

The horizontal and vertical flammability studies as per UL-94 for PP and its hybrid composites are summarized in Table 6. The rate of burning was calculated to be 29.12 mm/min and 27.87 mm/min for PP matrix and PPS27C3 hybrid composite, respectively. Furthermore, the rate of burning for PPS27C3M5 additionally reduced to 25.65 mm/min which indicates the addition of SiF and CNC reduces the burning rate irrespective of the dripping behavior which was witnessed in both the hybrid composites. PPS27C3M5 hybrid composite displayed the lowest rate of burning which is perhaps due to the formation of the covalent linkages at the interface in the presence of MAPP, hence increasing the flame resistance. The hybrid composites burn continuously with an orange-yellow flame while producing slight smoke and ignited the cotton. Further, the burning behavior was examined more precisely by conducting the vertical flammability study. All the samples burnt continuously up to the clamp holder after the 10 s of the application of flame. It demonstrated that the PP and its both hybrid composites exhibited a dripping behavior that prevents them to be measured for V-0, V-1, and V-2 grading [53].

### Conclusion

In the current study, the mechanical, morphological, thermal, viscoelastic, and flammability properties of the PP/SiF/CNC and PP/SiF/CNC/MAPP hybrid composites have been examined. PP hybrid composites fabricated at 27 wt% of SiF and 3 wt% of CNC loading with 5 wt% MAPP exhibited optimum mechanical performance. Several analytical models such as Cox–Krenchel and Ouali method in combination with Halpin–Tsai have been studied for the estimation of the theoretical elastic moduli. However, the estimated theoretical values deviated from the experimentally obtained values for both untreated and treated hybrid composites. Morphological observations confirmed a uniform dispersion of SiFs and



CNCs in the case of PPS27C3M5 nanocomposites. Conversely, PPS27C3 hybrid composites revealed agglomeration and voids in the impact fractured surface. DSC measurements observed no appreciable changes in  $T_m$  of PP in the PP hybrid composites system. However,  $T_c$  of the PP matrix increased in the case of hybrid composites due to the addition of SiFs and CNCs which acts as nucleation agents during the crystallization process. TGA studies shown higher thermal stability of PPS27C3M5 as compared to PP matrix and PPS27C3 hybrid composites. An optimum  $E'$  was depicted for PPS27C3M5 hybrid composites as evident by DMA studies.  $\tan \delta$  curve displayed  $\alpha$ - and  $\beta$ -transition of PP in their respective hybrid composite systems with a positive shift of  $T_g$  by the addition of microfibers and nanofillers.

## References

1. Dhand V, Mittal G, Rhee KY, Park S-J, Hui D (2015) A short review on basalt fibers reinforced polymer composites. *Compos Part B Eng* 73:166–180
2. Czigány T (2006) Special manufacturing and characteristics of basalt fiber reinforced hybrid polypropylene composites: mechanical properties and acoustic emission study. *Compos Sci Technol* 66(16):3210–3220
3. Nayak SK, Mohanty S, Samal SK (2009) Influence of short bamboo/glass fibers on the thermal, dynamic mechanical and rheological properties of polypropylene hybrid composites. *Mater Sci Eng A* 523:32–38
4. Saba N, Tahir PM, Jawaid M (2014) A review on potentiality of nano filler/natural fiber filled polymer hybrid composites. *Polymers (Basel)* 6:2247–2273
5. Kaewkuk S, Sutapun W, Jarukumjorn K (2013) Effects of interfacial modification and fibers content on physical properties of sisal fibers/polypropylene composites. *Compos Part B Eng* 45:544–549
6. Joseph K, Thomas S, Pavithran C, Brahmakumar M (1993) Tensile properties of short sisal fiber-reinforced polyethylene composites. *J Appl Polym Sci* 47(10):1731–1739
7. Mohanty S, Verma SK, Nayak SK, Tripathy SS (2004) Influence of fibers treatment on the performance of sisal-polypropylene composites. *J Appl Polym Sci* 94:1336–1345
8. Fu SY, Lauke B, Mäder E, Yue CY, Hu X (2000) Tensile properties of short-glass-fiber-and short-carbon-fiber-reinforced polypropylene composites. *Compos A Appl Sci Manuf* 31(10):1117–1125
9. Kumar S, Doshi H, Srinivasarao M, Park JO, Schiraldi DA (2002) Fibers from polypropylene/nano carbon fiber composites. *Polymer* 43(5):1701–1703
10. Samal SK, Mohanty S, Nayak SK (2009) Banana/glass fibers-reinforced polypropylene hybrid composites: fabrication and performance evaluation. *Polym Plast Technol Eng* 48:397–414
11. Rahman NA, Hassan A, Yahya R, Lafia-Araga R, Hornsby P (2012) Polypropylene/glass fibers/nanoclay hybrid composites: morphological, thermal, dynamic mechanical and impact behaviours. *J Reinf Plast Compos* 31:1247–1257
12. Samal SK, Mohanty S, Nayak SK (2009) Polypropylene—bamboo/glass fiber hybrid composites: fabrication and analysis of mechanical, morphological, thermal, and dynamic mechanical behaviour. *J Reinf Plast Compos* 28(22):2729–2747
13. Botev M, Betchev H, Bikiaris D, Panayiotou C (1999) Mechanical properties and viscoelastic behaviour of basalt fibers-reinforced polypropylene. *J Appl Polym Sci* 74:523–531
14. Yang HS, Gardner DJ, Nader JW (2011) Characteristic impact resistance model analysis of cellulose nanofibril-filled polypropylene composites. *Compos Part A Appl Sci Manuf* 42:2028–2035
15. Bahar E, Ucar N, Onen A, Wang Y, Oksüz M, Ayaz O, Ucar M, Demir A (2012) Thermal and mechanical properties of polypropylene nanocomposite materials reinforced with cellulose nano whiskers. *J Appl Polym Sci* 125(4):2882–2889

16. Peng Y, Gallegos SA, Gardner DJ, Han Y, Cai Z (2016) Maleic anhydride polypropylene modified cellulose nanofibril polypropylene nanocomposites with enhanced impact strength. *Polym Compos* 37(3):782–793
17. Gwon JG et al (2018) Physicochemical and mechanical properties of polypropylene-cellulose nanocrystal nanocomposites: effects of manufacturing process and chemical grafting. *BioResources* 13:1619–1636
18. Foulk JA, Chao WY, Akin DE, Dodd RB, Layton PA (2006) Analysis of flax and cotton fibers fabric blends and recycled polyethylene composites. *J Polym Environ* 14:15–25
19. Khan MA, Ganster J, Fink HP (2009) Hybrid composites of jute and man-made cellulose fibers with polypropylene by injection moulding. *Compos Part A Appl Sci Manuf* 40:846–851
20. Idicula M, Joseph K, Thomas S (2010) Mechanical performance of short banana/sisal hybrid fibers reinforced polyester composites. *J Reinforc Plast Compos* 29:12–29
21. Josefsson G, Berthold F, Gamstedt EK (2014) Stiffness contribution of cellulose nanofibrils to composite materials. *Int J Solids Struct* 51:945–953
22. Gogoi R, Manik G, Arun B (2019) High specific strength hybrid polypropylene composites using carbon fiber and hollow glass microspheres: development, characterization and comparison with empirical models. *Compos Part B Eng* 173:106875
23. Gupta MK, Choudhary N, Agrawal V (2018) Static and dynamic mechanical analysis of hybrid composite reinforced with jute and sisal fibres. *J Chin Adv Mater Soc* 6(4):666–678
24. Alshammari BA, Saba N, Alotaibi MD, Alotibi MF, Jawaid M, Alotman OY (2019) Evaluation of mechanical, physical, and morphological properties of epoxy composites reinforced with different date palm fillers. *Materials* 12(13):2145
25. Agarwal J, Sahoo S, Mohanty S, Nayak SK (2019) Progress of novel techniques for lightweight automobile applications through innovative eco-friendly composite materials: a review. *J Thermoplast Compos Mater* 3:12
26. Hanan F, Jawaid M, Md Tahir P (2020) Mechanical performance of oil palm/kenaf fiber-reinforced epoxy-based bilayer hybrid composites. *J Nat Fibers* 17(2):155–167
27. Dhar P, Tarafder D, Kumar A, Katiyar V (2015) Effect of cellulose nanocrystal polymorphs on mechanical, barrier and thermal properties of poly(lactic acid) based bionanocomposites. *RSC Adv* 5:60426–60440
28. Thomason JL, Vlugg MA (1997) Influence of fiber length and concentration on the properties of glass fiber-reinforced polypropylene: 4. Impact properties. *Compos Part A Appl Sci Manuf* 28:277–288
29. Vilaseca F et al (2012) Analysis of the tensile modulus of polypropylene composites reinforced with stone groundwood fibers. *BioResources* 7:1310–1323
30. Nishino T et al (2003) Elastic modulus of the crystalline regions of cellulose triesters. *J Polym Sci Part B Polym Phys* 33:611–618
31. Siregar JP, Salit MS, Rahman MZA, Dahlan KZHM (2011) Thermogravimetric analysis (TGA) and differential scanning calorimetric (DSC) analysis of pineapple leaf fibre (PALF) reinforced high impact polystyrene (HIPS) composites. *Pertanika J Sci Technol* 19(1):161–170
32. Kalaprasad G, Joseph K, Thomas S (1997) Influence of short glass fibers addition on the mechanical properties of sisal reinforced low density polyethylene composites. *J Compos Mater* 31:509–527
33. Yang HS et al (2004) Rice-husk flour filled polypropylene composites; mechanical and morphological study. *Compos Struct* 63:305–312
34. Tarrés Q et al (2019) Interface and micromechanical characterization of tensile strength of bio-based composites from polypropylene and henequen strands. *Ind Crops Prod* 132:319–326
35. Keener T, Stuart R, Brown T (2004) Maleated coupling agents for natural fiber composites. *Compos Part A Appl Sci Manuf* 35:357–362
36. Rezaei F, Yunus R, Ibrahim NA, Mahdi ES (2008) Development of short-carbon-fibers-reinforced polypropylene composite for car bonnet. *Polym. Plast Technol Eng* 47:351–357
37. Weiss RA (1981) Mechanical properties of polypropylene reinforced with short graphite fibers. *Polym Compos* 2(3):95–101
38. Fu SY, Xu G, Mai YW (2002) On the elastic modulus of hybrid particle/short-fibers/polymer composites. *Compos Part B Eng* 33:291–299
39. Biswal M, Mohanty S, Nayak SK (2009) Influence of organically modified nanoclay on the performance of pineapple leaf fibers-reinforced polypropylene nanocomposites. *J Appl Polym Sci* 114(6):4091–4103

40. Xu N, Ding E, Xue F (2017) Influence of particle size of isotactic polypropylene (iPP) on barrier property against agglomeration of homogenized microcrystalline cellulose (HMCC). *iPP HMCC Compos* 38(3):213–222. <https://doi.org/10.1515/polyeng-2017-0004>
41. Azeredo HM, Mattoso LHC, Wood D, Williams TG, Avena-Bustillos RJ, McHugh TH (2009) nanocomposite edible films from mango puree reinforced with cellulose nanofibers. *J Food Sci* 74(5):N31–N35
42. Johari AP, Mohanty S, Kurmvanshi SK, Nayak SK (2016) Influence of different treated cellulose fibers on the mechanical and thermal properties of poly(lactic acid). *ACS Sustain Chem Eng* 4:1619–1629
43. Heux L (2006) Nanocomposites of isotactic polypropylene reinforced with rod-like cellulose whiskers. *Polymer* 47:6285
44. Matei E et al (2017) Recycled polypropylene improved with thermoplastic elastomers. *Int J Polym Sci* 2017:17
45. Espert A, Camacho W, Karlson S (2003) Thermal and thermomechanical properties of biocomposites made from modified recycled cellulose and recycled polypropylene. *J Appl Polym Sci* 89:2353–2360
46. Kim SH et al (2019) Rheological and mechanical properties of polypropylene composites containing microfibrillated cellulose (MFC) with improved compatibility through surface silylation. *Cellulose* 26:1085–1097
47. Unterweger C, Brüggemann O, Fürst C (2014) Effects of different fibers on the properties of short-fibers-reinforced polypropylene composites. *Compos Sci Technol* 103:49–55
48. Kotzev G, Djoumalitsky S, Natova M, Benavente R (2012) Vibration-assisted melt compounding of polypropylene/carbon black composites: processability, filler dispersion and mechanical properties. *J Reinf Plast Compos* 31:1353–1363
49. Cichosz S, Masek A, Wolski K, Zaborski M (2019) Universal approach of cellulose fibers chemical modification result analysis via commonly used techniques. *Polym Bull* 76:2147–2162
50. Hassan ML, Mathew AP, Hassan EA, Fadel SM, Oksman K (2014) Improving cellulose/polypropylene nanocomposites properties with chemical modified bagasse nanofibers and maleated polypropylene. *J Reinf Plast Compos* 33:26–36
51. Kitano T, Hashmi SAR, Chand N (2004) Influence of steady shear flow on dynamic viscoelastic properties of un-reinforced and Kevlar, glass fiber reinforced LLDPE. *Bull Mater Sci* 27:409–415
52. Amash A, Zugenmaier P (1997) Thermal and dynamic mechanical investigations on fibers-reinforced polypropylene composites. *J Appl Polym Sci* 63(9):1143–1154
53. Younis AA (2017) Flammability properties of polypropylene containing montmorillonite and some of silicon compounds. *Egypt J Pet* 26:1–7

**Publisher's Note** Springer Nature remains neutral with regard to jurisdictional claims in published maps and institutional affiliations.